Impact of late spring Siberian snow on summer rainfall in South-Central China

Haibo Shen[1,2] · Fei Li[1,3] · Shengping He[1,3] · Yvan J. Orsolini[4] · Jingyi Li[1]

Abstract

Located in the Yangtze River Valley and surrounded by mountains, South-Central China (SCC) frequently suffered from natural disasters such as torrential precipitation, landslide and debris flow. Here we provide corroborative evidence for a link between the late spring (May) snow water equivalent (SWE) over Siberia and the summer (July–August, abbr. JA) rainfall in SCC. We show that, in May, anomalously low SWE over Siberia is robustly related to a large warming from the surface to the mid-troposphere, and to a stationary Rossby wave train from Siberia eastward toward the North Atlantic. On the one hand, over the North Atlantic there exhibits a tripole pattern response of sea surface temperature anomalies in May. It persists to some extent in JA and in turn triggers a wave train propagating downstream across Eurasia and along the Asian jet, as the so-called Silk Road pattern (SRP). On the other hand, over northern Siberia the drier soil occurs in JA, accompanied by an overlying anomalous anticyclone through the positive feedback. This anomalous anticyclone favors the tropospheric cooling over southern Siberia, and the meridional (northward) displacement of the Asian jet (JMD) due to the change in the meridional temperature gradient. The combination of the SRP and the JMD facilitates less water vapor transport from the tropical oceans and anomalous descending motion over SCC, and thus suppresses the precipitation. These findings indicate that May Siberian SWE can be exploited for seasonal predictability of SCC precipitation.

Keywords Siberian snow water equivalent · Precipitation in South-Central China · Sea surface temperature over the North Atlantic · Siberian soil moisture · The Silk Road pattern · The meridional displacement of the Asian jet

1 Introduction

The mountainous areas drained by the Yangtze River and its tributaries (i.e., Yangtze River Valley, abbr. YRV) are regions of rapid economic development and population growth at great risk from natural disasters. Particularly, South-Central China (SCC) is highly susceptible to extreme flooding and drought events. For example, SCC suffered from the extreme drought and heat wave of the summer 2013, which affected about 47.8 million people, 3.63 million livestock and 48 thousand km^2 arable land and caused direct economic losses up to ¥30 billion (Duan et al. 2013).

Previous studies demonstrated that the sea surface temperature anomalies (SSTAs) over the tropical Pacific Ocean, the tropical Indian Ocean as well as over the north Atlantic Ocean, give rise to changes in summer rainfall over SCC. Traditionally, the strongly coupled sea-air interactions in the tropics, known as the El Niño–Southern Oscillation (ENSO), is a notable external forcing of the summer rainfall variability over SCC, in which a long-maintained,

✉ Haibo Shen
  shb1992@126.com

[1] Collaborative Innovation Center on Forecast and Evaluation of Meteorological Disasters/Key Laboratory of Meteorological Disaster, Ministry of Education, Nanjing University of Information Science and Technology, Nanjing, China

[2] Power Dispatching Control Center, China Southern Power Grid Company Limited, Guangzhou, China

[3] Geophysical Institute, University of Bergen and Bjerknes Centre for Climate Research, Bergen, Norway

[4] NILU - Norwegian Institute for Air Research, Kjeller, Norway

lower-tropospheric anticyclone over the Philippines causes more moisture transport along its western boundary (Wang et al. 2000; Huang et al. 2004). It is noteworthy that the relationship between ENSO and the summer rainfall over SCC is not stable on the multidecadal timescales (Wang 2002). Over the analysis period of 1964–1995 in Wang (2002), significant correlation emerges only during 1964–1974 and 1983–1990, when there is large interannual variability of the low-level temperature and of the subtropical high over the tropical Pacific. Additionally, Shen et al. (2019) found the reverse August precipitation anomaly over eastern China in 1998 and 2016, which are both the super El Niño events in history. Early studies also emphasized that the tropical Indian Ocean (TIO) SST acts as a capacitor, anchoring the suppressed convection and lower-tropospheric anticyclone over the Philippines during the El Niño decay phase (Yang et al. 2007; Xie et al. 2009). Moreover, it has been documented that the tripole pattern of the North Atlantic SSTAs and the phase of the North Atlantic Oscillation (NAO) modulate the summer rainfall variability over SCC, via triggering a stationary Rossby wave train extending from the North Atlantic toward East Asia (Sung et al. 2006; Linderholm et al. 2011; Tian and Fan 2012). Land surface conditions, such as soil moisture, also influence the summer rainfall variability over SCC (Zhang and Zuo 2011; Meng et al. 2014). Drier soil conditions in spring, stretching from the Yangtze River valley to North China, increase the surface air temperature and hence strengthen the East Asian summer monsoon (EASM) and summer rainfall over SCC by enhancing the sea-land thermal difference (Zhang and Zuo 2011). Halder and Dirmeyer (2017) demonstrated that negative soil moisture anomalies over eastern Eurasia in spring induce an anomalous upper-tropospheric ridge around 100° E via anomalous surface and mid-tropospheric heating, which further modulates the Asian jet and summer rainfall over Asia.

Snow is another important land surface factor that exerts a strong control on the overlying atmosphere and even on the hemispheric-scale circulation. Via the radiative snow-albedo feedback and the thermodynamical feedback (the insulating snow layer decoupling the lower atmosphere from the soil), a thicker snowpack (or higher snow water equivalent, SWE) cools the lowermost atmosphere (Walsh et al. 1985; Groisman et al. 1994). In addition, there is the hydrological feedback whereby positive (negative) snow anomalies convert in positive (negative) soil moisture anomalies with a delay, in the melting season. Previous studies demonstrated that an anomalous Siberian snow cover can be accompanied by polar vortex and northern annular mode anomalies during autumn and winter, coupling the troposphere to the stratosphere (Cohen et al. 2007; Fletcher et al. 2009; Henderson et al. 2018). The snowpack can have significant impacts on the atmospheric circulation not only during the contemporaneous season but also in the following seasons. Based upon

the observational analyses, many studies found a negative correlation between the spring or summer Siberian snow cover/depth and the strength of the Indian summer monsoon through the combination of radiative, thermodynamical and hydrological feedbacks (e.g. Hahn and Shukla 1976; Dickson 1984; Bamzai and Shukla 1999; Fasullo 2004; Dash et al. 2005). The impact and the mechanism have also been revealed by the numerical models (Yasunari et al. 1991; Bamzai and Marx 2000; Dash et al. 2006).

Some studies specifically explored the impact of the Siberian snow on the East Asian summer rainfall. Based on the singular value decomposition (SVD) analysis, the SWE over Eurasia during spring derived from National Snow and Ice Center (NSIDC) has been linked to the summer rainfall in China during the period of 1979–2004 (Wu et al. 2009). By using the empirical orthogonal function (EOF) analysis for snow cover data from NOAA satellites, Yim et al. (2010) noted that the east–west dipole mode of snow cover anomalies (with the positive and negative values over western and eastern Eurasia, respectively) is closely related to the EASM during 1972–2004. But the significant summer rainfall anomalies associated with this dipole were only observed over Korea and Japan, not over eastern China. Analyzing the period of 1979–2013, Zhang et al. (2017) found that the east–west dipole mode of the spring SWE decrement (SWE in February minus SWE in May) is associated with the summer rainfall over East Asia through the local Eurasian soil conditions persisting from spring to summer. However, Robock et al. (2003) argued that the soil moisture alone could not explain the impact of the preceding Eurasian snow on the summer precipitation over Asia. While a moderate relationship between SWE over Siberia in May and rainfall over China in summer was found in reanalysis and seasonal reforecasts during 1983–2010 (Zuo et al. 2015), the linking mechanism was not elucidated. Though the Siberian snow is suggested to have a significant impact on the Asian summer climate, these studies have suffered from several limitations. (1) The analysis period is relatively short. Most previous studies only covered the period ending in the early twenty-first century. (2) There is uncertainty in the snow observations. For example, snow cover is derived from optical and infrared remote sensing by the NOAA satellites, and there is uncertainty associated with the conversion of binary pixel information about snow cover to large-scale snow cover gridded data. On the other hand, the widely used SWE data provided by the NSIDC is derived from microwave remote sensing, and there is inaccuracy due to the retrieval method using a static algorithm (Xu et al 2018); (3) Although Zhang et al. (2017) pointed out the importance of the snow persistent influence into the summer through the hydrological feedback for maintaining eastward-propagating wave trains across Eurasia, the relative roles of SST and land conditions have not been fully clarified.

The present study investigates the potential linkage between late spring (May) SWE over Siberia and summer (July–August) rainfall in SCC for the period 1979–2018, based on SWE and soil moisture data retrieved from the ECMWF (European Centre for Medium-Range Weather Forecasts) Interim/Land reanalysis (with more information in Sect. 2). The important roles played by the North Atlantic SST and Siberian soil moisture to perdure the influence of the spring Siberian snow into the summer season and to connect the latter with precipitation over SCC are explored quantitatively.

2 Data, climatic indices and methods

This study utilizes five datasets. The monthly (1) SWE and (2) soil moisture in three layers (7 cm, 21 cm, 72 cm) are obtained from the ERA-Interim/Land with a resolution of $1° \times 1°$ (Balsamo et al. 2015). (3) The monthly and daily atmospheric fields are collected from the ERA-Interim reanalysis, with a horizontal resolution of $1° \times 1°$ (Dee et al. 2011). (4) The monthly precipitation data are retrieved out of the monthly mean CPC Merged Analysis of Precipitation (CMAP), which are available in a $2.5° \times 2.5°$ grid (Xie and Arkin 1997). (5) The monthly SST data are provided by the Met Office Hadley Centre (Rayner et al. 2003), with a resolution of $1° \times 1°$. The analyzed period in this study covers from 1979 to 2018.

The ERA-interim/land snow data is a high spatial resolution reanalysis driven by realistic meteorological forcing. Wegmann et al. (2017) has validated the ERA-interim/land reanalysis against the in-situ station data over northern Russia. The Taylor diagram (their Fig. 5) displays the daily variability of snow depth in ERA-interim/land against the in-situ observation over 13 Russian stations over the period 1981–2010, in which their correlation is 0.8 in April and their standard deviations are comparable. Moreover, we validate the SWE data in the ERA-interim/land against the relatively long-period, satellite-based SWE dataset from the Finnish Meteorological Institute (FMI), with a spatial resolution of 25 km from 1979 to 2014 (Takala et al. 2011; see detailed information at http://www.globsnow.info/). The SWE product from FMI combines satellite-based passive microwave measurements with ground-based weather station data in a data assimilation scheme. For the interannual variability, the ERA-interim/land data is highly consistent with the FMI data over Siberia (Fig. S1a). The spatial distributions of the SWE climatology from the FMI data and the ERA-interim/land data are quite similar, though the ERA-interim/land data overestimate the magnitude of the SWE over the Central and East Siberian Plateaus (Fig. S1b). Taken together, it confirms that the ERA-interim/land reanalysis is an appropriate dataset that can be used in this study.

The definitions of the climatic indices are given in Table 1. All indices are standardized. To isolate the influence of Siberian snow on the atmospheric circulation and precipitation at the interannual timescale, any linear trend has been removed prior to analysis from all the indices and fields. The statistical methods used in the current study include correlation analysis, linear regression and SVD analysis. The statistical significance of correlation and regression is assessed using the two-tailed Student's t test. To illustrate the wave-like activity, the wave activity flux (WAF) is applied in the study (Takaya and Nakamura 2001). In order to diagnose the excitation of Rossby waves, the wave source term defined as $-\nabla \cdot \vec{V}_x (f + \zeta)$ (Sardeshmukh and Hoskins 1988) is calculated, where $\vec{V}_x$ is the divergent wind velocity, f is the Coriolis parameter, and ζ is the relative vorticity. The Siberian SWE (50°–75° N, 60°–140° E) in May is emphasized in this study with the largest interannual variability (Fig. S2). Additionally, the Siberian snow melts a lot in May, except for a few regions at very high altitudes or along the Arctic coast (Xu and Dirmeyer 2013). The spatial distribution of precipitation variations over China in June and July–August are distinct: the largest variability is located

Table 1 The indices and definitions

Indices	Month	Full name	Definitions
SWEI	May	Snow water equivalent index	SWE, SVD-PC1 of the May SWE and JA precipitation
SSTI	July–August	Sea surface temperature index	SST, [30°–42° N, 54°–74° W]–[35°–45° N, 28°–45° W]
SMI	July–August	Soil moisture index	SM, [63°–72° N, 100°–125° E]
STMI	July–August	Sea surface temperature-soil moisture index	Corr. (SMI, SWEI) × SMI + Corr. (SSTI, SWEI) × SSTI
JMDI	July–August	Jet meridional displacement index	200 hPa U, [40°–55° N, 40°–150° E]–[25°–40° N, 40°–150° E]
SRPI	July–August	Silk road pattern index	EOF-PC1 of V200 over (20°–60° N, 60° W–130° E)
PI	July–August	Precipitation index	Precipitation (multiplied by −1), averaged over the frame in Fig. 1b (South-Central China)

Square brackets represent the area-mean

over South China Sea and over Yangtze River Valley, respectively (Wang et al. 2009, their Fig. 4). Hence, in the current study, we focus on the precipitation during the late summer (July–August) rather than the 3-month (June–August) mean.

3 Results

3.1 The relationship between May SWE over Siberia and summer precipitation over South-Central China

Figure 1 illustrates the leading SVD mode for the May SWE over Siberia and the July–August (JA) precipitation over eastern China. The leading mode accounts for 18.8% of the total interannual variance of the Siberian SWE anomalies in May. Notable are negative SWE anomalies over Siberia in May, especially over central and eastern regions (Fig. 1a). Meanwhile, there are below-normal precipitation in JA over parts of the Inner Mongolia and YRV, particularly over SCC (Fig. 1b). The corresponding time series (Fig. 1c) indicates a statistically significant linkage between Siberian SWE in May and summer precipitation over SCC, with a coefficient of 0.81 (above the 99% confidence level). Here we define the SWE index (SWEI)

using the normalized time series of the SWE variations in the leading SVD mode (positive SWEI corresponds to reduced SWE over Siberia). The area-averaged precipitation anomalies over SCC (the frame marked in Fig. 1b), multiplied by -1, is taken as the precipitation index (PI), implying that a positive value indicates below-normal precipitation. As expected, the correlation coefficient between SWEI and PI is 0.48 (Fig. 2a; above 99% confidence level). It is noteworthy that these results can be reproduced by using the SWE data from the FMI (Fig. S3).

Figure 2b illustrates the water vapor flux anomalies integrated vertically from 1000 to 300 hPa in JA regressed onto the SWEI. The water fluxes are indicative of an anomalous anticyclone over the western North Pacific (35° N), implying a westward-extended western Pacific subtropical high (Fig. 2b: vectors). At lower latitudes (20° N), around 120° E, they are also indicative of an anomalous cyclonic circulation over southeastern China, with the northerly flow decreasing the water vapor flux from the tropical oceans to SCC (Fig. 2b: vectors), resulting in significantly positive divergence anomalies in SCC (Fig. 2b: shading and frame). Besides, the meridional-vertical cross section of vertical velocity anomalies regressed upon the SWEI, averaged between 105°–120° E (Fig. 2c), shows anomalous descending motion around 25°–32° N throughout the
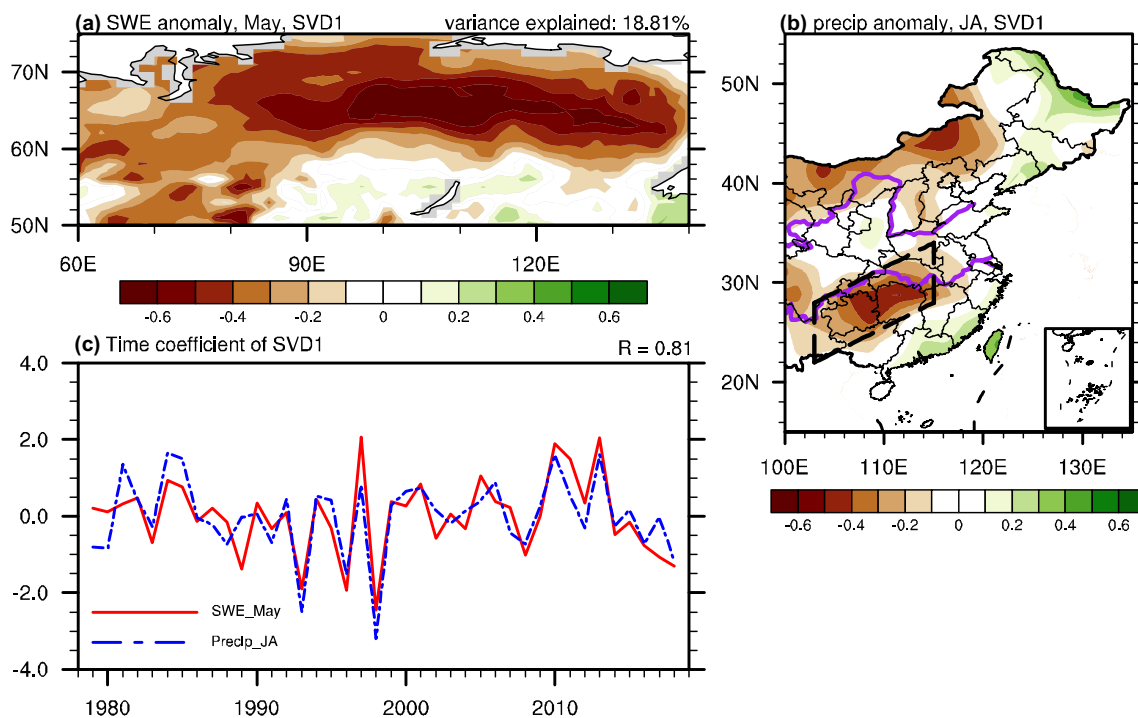
Fig. 1 Spatial distributions of detrended and normalized **a** snow water equivalent (SWE) in May over Siberia and **b** precipitation in July–August (JA) over eastern China of the leading SVD mode for 1979–2018. **c** The corresponding time series of the May SWE pattern (red solid line) and the JA precipitation pattern (blue dash line),

with a positive value indicating the snow/precipitation decrease. In **b**, the purple curves denote the Yangtze River and Yellow River, respectively, and the region marked by dashed lines denotes the South-Central China here and hereafter
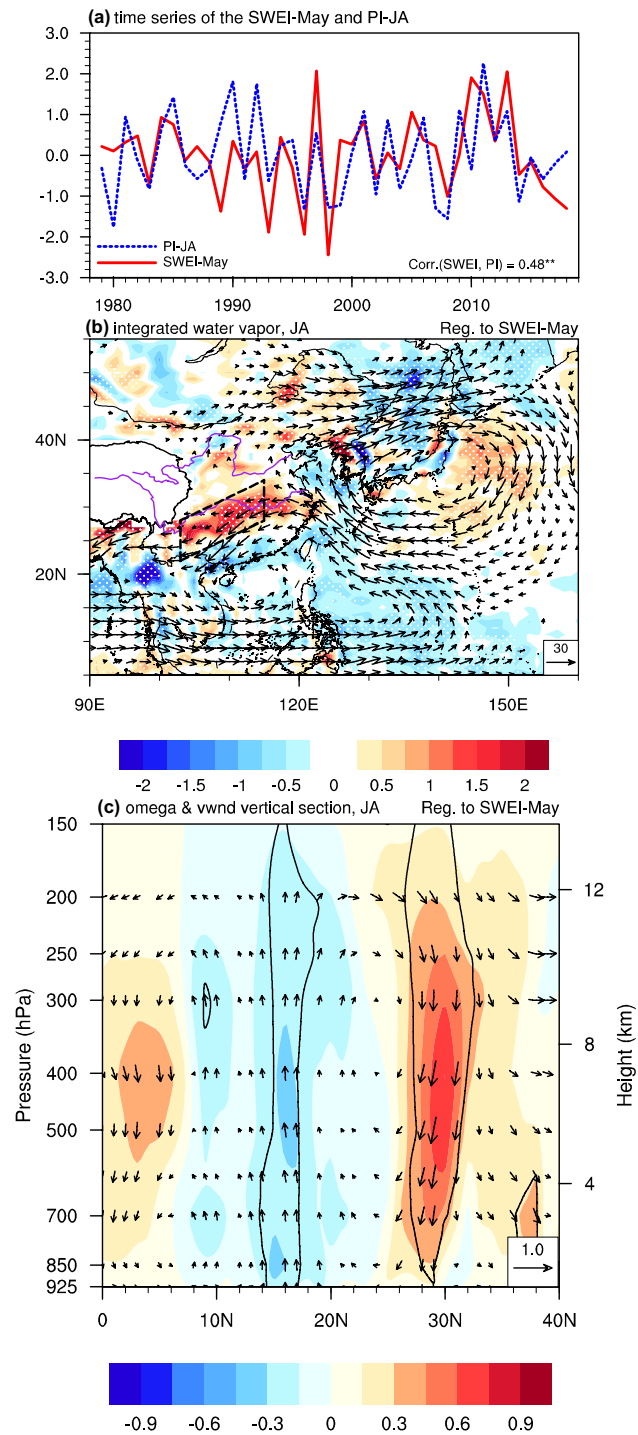
Fig. 2 a The time series of the snow water equivalent index (SWEI) in May (red solid line) and the precipitation index (PI) in JA (blue dash line). **b–c** Regressions of **b** vertically-integrated water vapor flux (from 1000 to 300 hPa; vectors; kg m^{-1} s^{-1}) and its divergence (shading; 10^{-5} kg m^{-2} s^{-1}) anomalies in JA, and **c** meridional-vertical cross section averaged along 105°–120° E for the vertical wind (vectors; m s^{-1}) and omega (shading; 10^{-2} Pa s^{-1}) anomalies in JA, upon the SWEI in May during 1979–2018. Data over the Tibetan Plateau in **b** is masked out and the shape of the Tibetan Plateau is derived from Zhang et al. (2002). Values stippled in **b** and enclosed by the black contours in **c** are significant at the 90% confidence level, based on the Student's *t* test

entire troposphere. Taken together, less SWE over Siberia in May is robustly linked to positive water vapor flux divergence anomalies and anomalous descending motion, which suppresses the summer precipitation over SCC.

3.2 The influences of the preceding Siberian SWE in May

Previous studies have revealed that variation of snow conditions has an impact at the surface and in the troposphere via radiative, hydrological and thermodynamical effects (e.g. Barnett et al. 1989; Cohen and Rind 1991; Dash et al. 2005; Sun 2017). Figure 3a shows the SWE, tropospheric air temperature and zonal wind anomalies in May along the 120° E meridian regressed onto the SWEI. Corresponding to the significantly negative SWE anomalies over Siberia (between 60° N and 70° N), there is a significant warm-core in the lower-troposphere (Fig. 3a: shading), which may attribute to a positive surface sensible heat flux anomaly over Siberia (Fig. S4a). Besides, an anomalous anticyclone is apparent over the northern Siberia–North Pacific Sector through the snow–atmospheric coupling (Figs. S4b and 4c). Negative and positive zonal wind anomalies emerge in the southern and northern flanks of the anomalous warm-core anticyclone (Fig. 3a; contours). Xu and Dirmeyer (2011) has revealed the strong snow–lower atmosphere coupling over Siberia in May, and Xu and Dirmeyer (2013) further demonstrated that the vertical extent of this coupling is up to the mid-troposphere (500 hPa).

Figure 3b illustrates the geopotential height and horizontal WAF anomalies at 300 hPa in May regressed onto the SWEI. A largely positive geopotential height anomaly at 300 hPa is found over the Siberia–North Pacific sector in May, related to the reduced SWE, together with alternating negative and positive height anomalies downstream (Fig. 3b; contours). This signature is consistent with the formation of an apparent Rossby wave train stretching from the eastern North Pacific to western North America. It then ramifies into two branches: one propagates southward toward the lower latitudes, and the other extends eastward into the mid-latitude North Atlantic (120°–90° W). Notable is that the latter branch is observed stretching northeastward to Europe, resulting in a negative height anomaly center over western Europe (Fig. 3b: vectors). The aforementioned Rossby wave source (RWS) displays strong positive anomalies over Siberia (Fig. 4a). Previous studies suggested that the advection of vorticity by the divergent and convergent component of the upper tropospheric flow acts as an effective RWS (Sardeshmukh and Hoskins 1988; Chen and Huang 2012). Due to the weakened westerly wind induced by the thermal anomaly (Fig. 3a), the horizontal wind at 300 hPa converges over Siberia, generating a positive RWS anomaly through the
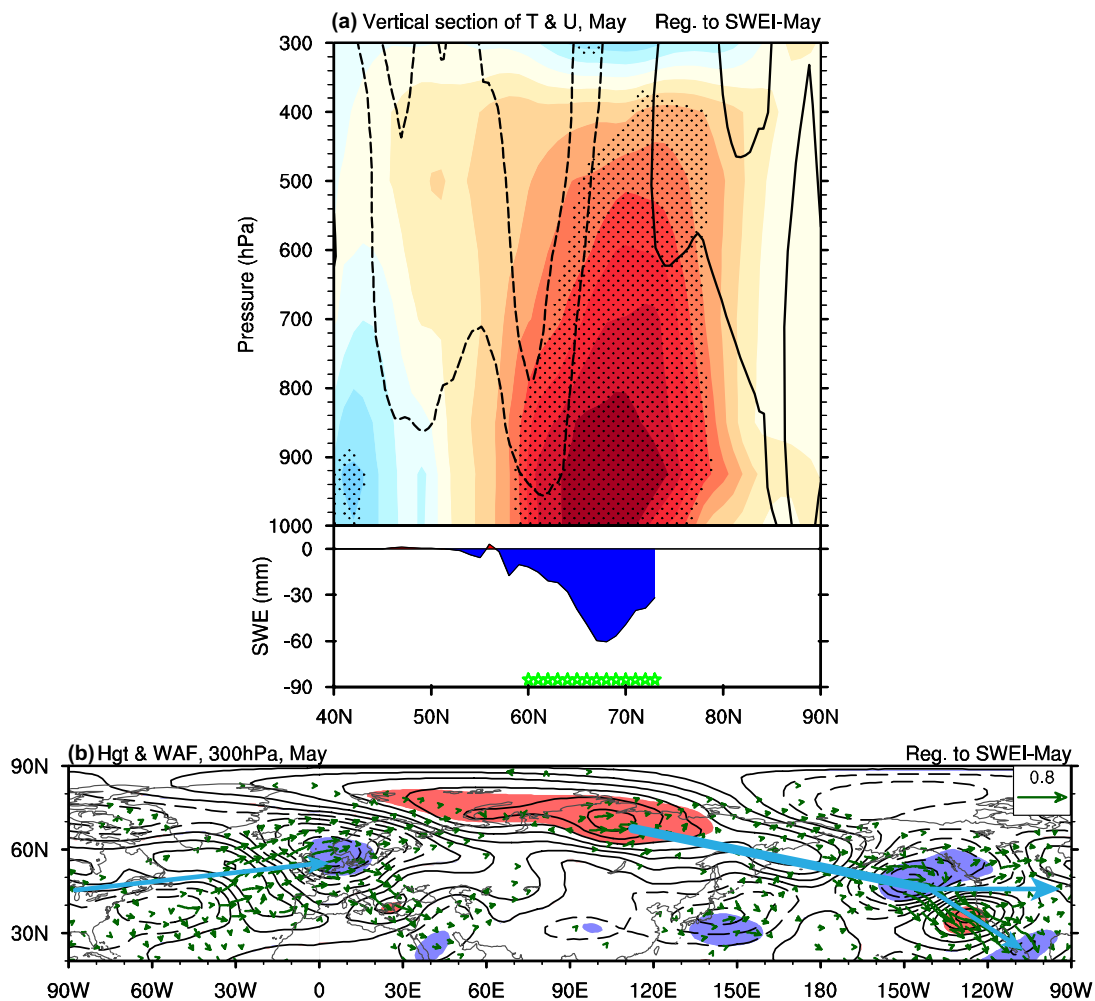
Fig. 3 Regressions of **a** meridional-vertical cross section along 120° E of temperature (upper panel; shading; K), zonal wind (upper panel; contours; m s^{-1}) and the underlying SWE (lower panel; mm) anomalies in May, and **b** geopotential height (contours; gpm) and associated horizontal wave activity fluxes (WAFs; vectors; m^2 s^{-2}) anomalies at 300 hPa in May, upon the SWEI in May during 1979–2018. Con-tours in **a** are at ± 0.4, ± 0.8, ± 1.2 m s^{-1} and in **b** are at ± 4, ± 8, …, ± 28 gpm. The thick blue arrows in **b** denote the Rossby wave trains. Stippled regions and green markers in **a**, and shading in **b** denote the values are significant at the 90% confidence level, based on the Student's t test

positive vorticity advection by the convergent flow (Fig. 4a, b). These results indicate that the SWE anomalies over Siberia are associated with eastward-propagating Rossby wave trains to the North Atlantic via the anomalous upper-level divergent flow.

Focusing on the North Atlantic in May, we note the meridionally banded structures of the zonal wind anomalies (Fig. 5a), with two bands negative anomalies around 45° N and 25° N and one band of positive anomaly between them. The results suggest the deceleration of both the eddy-driven (45° N) and subtropical (25° N) jets over the North Atlantic. The decelerated jets induce the easterly and south-erly wind anomalies near the surface, and further lead to the northern (50°–60° N, 30°–60° W) positive centers of the SSTAs (Fig. 5b: shading). In addition, the decelerated

westerly jet may also reinforce the meridional anomalies of the atmosphere. It appears the northerly wind anomaly to the south (30°–40° N, 40°–70° W), weakening the warming cur-rent from the Gulf Stream (Rossby 1996), which cools the underlying SST. The tripole pattern of SSTAs is thus appar-ent. Moreover, there is an in-phase relationship between the turbulent heat flux anomalies and the SSTAs, especially over the two SST anomaly centers: the negative SSTAs around 30°–40° N concur with the negative turbulent heat flux anomalies, and the positive SSTAs around 50°–60° N con-cur with the positive turbulent heat flux anomalies (Fig. 5b: contours). Positive turbulent heat flux anomalies represent downward flux, and this relation suggests that May SSTAs over the North Atlantic are mainly instigated by the atmos-phere (See vectors in Fig. 5b). In conclusion, less Siberian
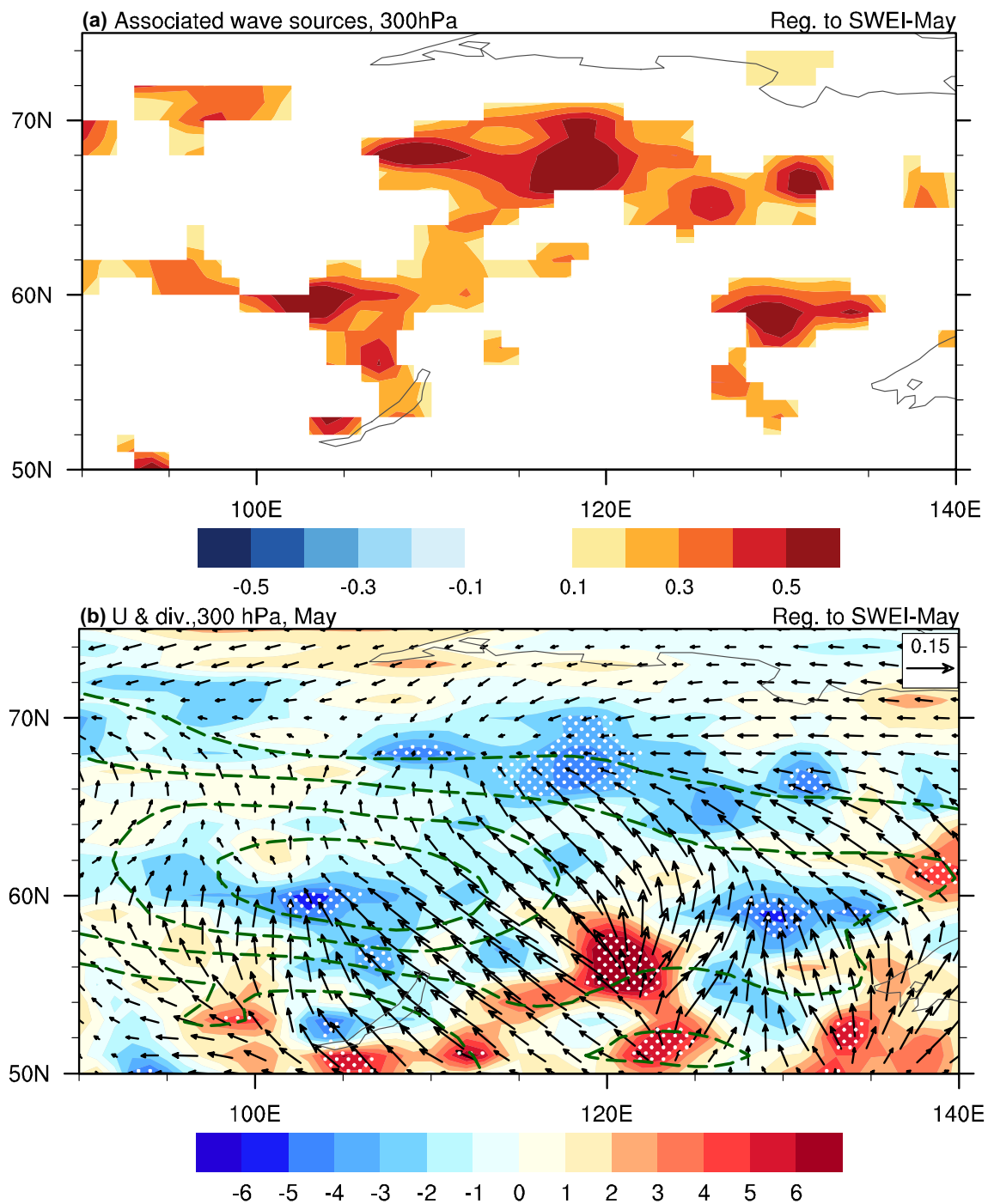
Fig. 4 Regressions of **a** Rossby wave source anomalies (10^{-10} s^{-2}, only values larger than 10^{-11} s^{-2} are shown) at 300 hPa in May, and **b** zonal wind (contours; m s^{-1}), divergent wind (vectors; m s^{-1}) and divergence (shading; 10^{-6} s^{-1}) anomalies at 300 hPa in May, upon the SWEI in May during 1979–2018. Stippled values in **b** are significant at the 90% confidence level, based on the Student's t test

SWE in May is associated with the local tropospheric warming up to 400 hPa, which induces a Rossby wave train propagating eastward toward the North Atlantic. The associated westerly jets over the North Atlantic decelerate, which further contributes to the tripole pattern of Atlantic SSTAs.

3.3 The connecting roles of the North Atlantic SST and Siberian soil moisture in JA

Figure 6a illustrates the SST and turbulent heat flux anomalies in JA regressed onto the SWEI. In comparison with Fig. 5b, the two anomaly centers of the SST over the mid-to

Fig. 5 Regressions of **a** the zonal wind (contours; m s^{-1}) at 300 hPa in May and **b** the SST anomalies (shading; K)/surface turbulent heat flux (contours; 10^5 J m^{-2})/horizontal wind at 1000 hPa (vectors; m s^{-1}) in May, upon the SWEI in May during 1979–2018. Contours in **b** are at ± 1, ± 3, ± 5 × 10^5 J m^{-2}. The positive turbulent heat flux means the downward flux and vice versa. Stippled values are significant at the 90% confidence level, based on the Student's t test. The green thick line in **a** delineates the axis of the climatological westerly jet here and hereafter
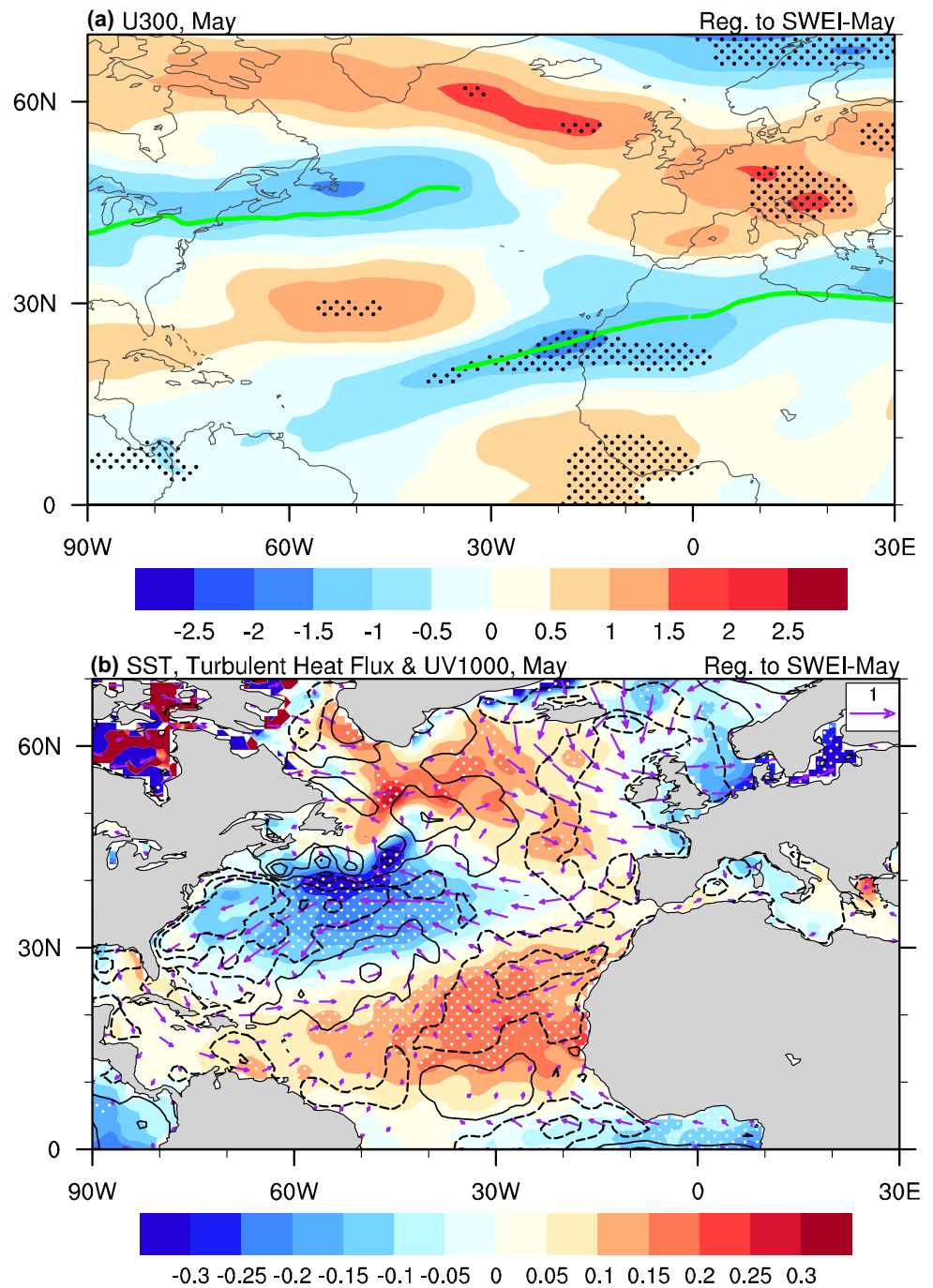
high-latitude North Atlantic persist. However, the significant anomaly center over the low-latitude North Atlantic northwestward shifts around the Gulf Stream. More interestingly, the relationship between the anomalous turbulent heat flux and the SSTAs becomes out-of-phase, especially over the two anomaly centers around 35° N and 45° N (the black frames in Fig. 6a). This out-of-phase relationship indicates that the SSTAs exert an influence onto the overlying atmosphere. Here the area-averaged SST in these two anomaly centers is used to define the North Atlantic

SST index (SSTI), and its correlation coefficient with the SWEI is 0.34 (above 95% confidence level; Fig. 6b). Figure 6c shows the 200 hPa horizontal wind anomalies in JA regressed onto the SSTI. There is a largely anomalous cyclone over the North Atlantic, accompanied with cyclonic and anticyclonic circulation anomalies downstream across Eurasia (Fig. 6c: vectors). Besides, the apparent positive and negative anomalies of the 200 hPa meridional wind indicate a wave train from the North Atlantic eastward to Eurasia (Fig. 6c: contours). From the North Atlantic, there are two
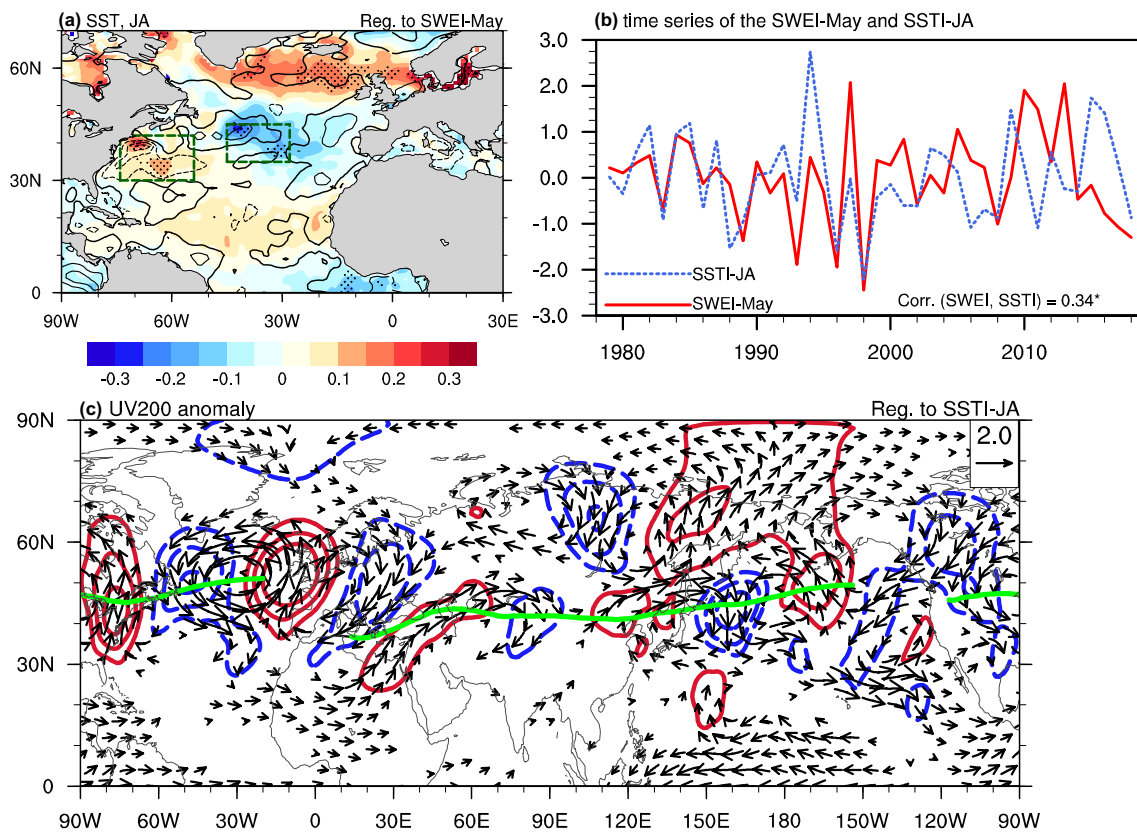
Fig. 6 **a** Regression of SST (shading; K) and turbulent heat flux (contours; 10^5 J m^{-2}) in JA, upon the SWEI in May during 1979–2018. **b** The time series of the SWEI in May (red solid line) and the sea surface temperature (SSTI) in JA (light blue dash line). **c** Regressions of 200 hPa meridional wind (contours; m s^{-1}) and horizontal wind (vectors; m s^{-1}) anomalies in JA, upon the SSTI in JA during 1979–2018. Contours in **a** are at ± 2, ± 4, $\pm 6 \times 10^5$ J m^{-2} and in **c** are at ± 0.5, ± 1.0, ± 1.5 gpm

Table 2 Correlation Coefficients of climatic indices

	SWEI	SSTI	SMI	STMI	JMDI	SRPI	PI
SWEI	—	0.34	0.36	0.46	0.36	0.16	0.48
SSTI	—	—	0.17	0.75	0.26	0.48	0.28
SMI	—	—	—	0.78	0.41	0.21	0.43
STMI	—	—	—	—	0.44	0.45	0.47
JMDI	—	—	—	—	—	0.33	0.38
SRPI	—	—	—	—	—	—	0.29
PI	—	—	—	—	—	—	—

The light, medium and dark red indicate statistical significance at the 90%, 95% and 99% confidence levels, respectively, based on the Student's *t* test

branches of the Rossby wave train over Eurasia: the Ural-Siberia route (northern branch) and the Mediterranean-East Asia route (southern branch; e.g. Orsolini et al., 2015). The latter one along the southern slope of the Tibetan Plateau and the climatological jet axis resembles the so-called Silk Road pattern (SRP; Lu et al. 2002; Hong and Lu 2016). The SRP index (see the definition in Table 1, referring to Chen and Huang 2012) is highly correlated with the SSTI, with a coefficient of 0.48 (above 99% confidence level, Table 2). Consistently, previous studies have pointed out that the SSTAs over the North Atlantic can excite the stationary wave train to East Asia (Gu et al. 2009; Tian and Fan 2012).

Further, we focus on the connecting role of the Siberian soil moisture. Figure 7a shows the top meter soil moisture anomalies in JA regressed onto the SWEI. A largely negative soil moisture anomaly occurs in most parts of Siberia, primarily because of less May Siberian SWE into June, but mainly confined to north of 65° N (Fig. S5). Hence, less SWE in May–June leads to less local melting in JA. We further define a soil moisture index based upon this negative center (SMI; multiplied by − 1, hence a positive value implying the drier soil moisture; Fig. 7b). The correlation of SMI and SWEI is 0.36 (Fig. 7b). There are also other localized positive (90° E and 130° E) and negative (65° E and 105° E) soil moisture anomalies alternatively over southern Siberia, which may be induced by the alternating anticyclonic and cyclonic anomalies along the Ural-Siberia wave route (Figs. 6c, 8b). Figure 7c illustrates the temperature advection at 850 hPa, the vertical integral of temperature from 1000 to 200 hPa and its meridional gradient in JA regressed

(a) Soil water, JA — Reg. to SWEI-May

(b) time series of the SWEI-May, SMI-JA and JMDI-JA

JMDI-JA
SMI-JA
SWEI-May

Corr. (SWEI, SMI) = 0.36*
Corr. (SMI, JMDI) = 0.41**
Corr. (SWEI, JMDI) = 0.36*

(c) Vertically integrated of Tem. & meridional gradient, T_{adv}, JA — Reg. to SMI-JA

(d) U300, JA — Reg. to SMI-JA
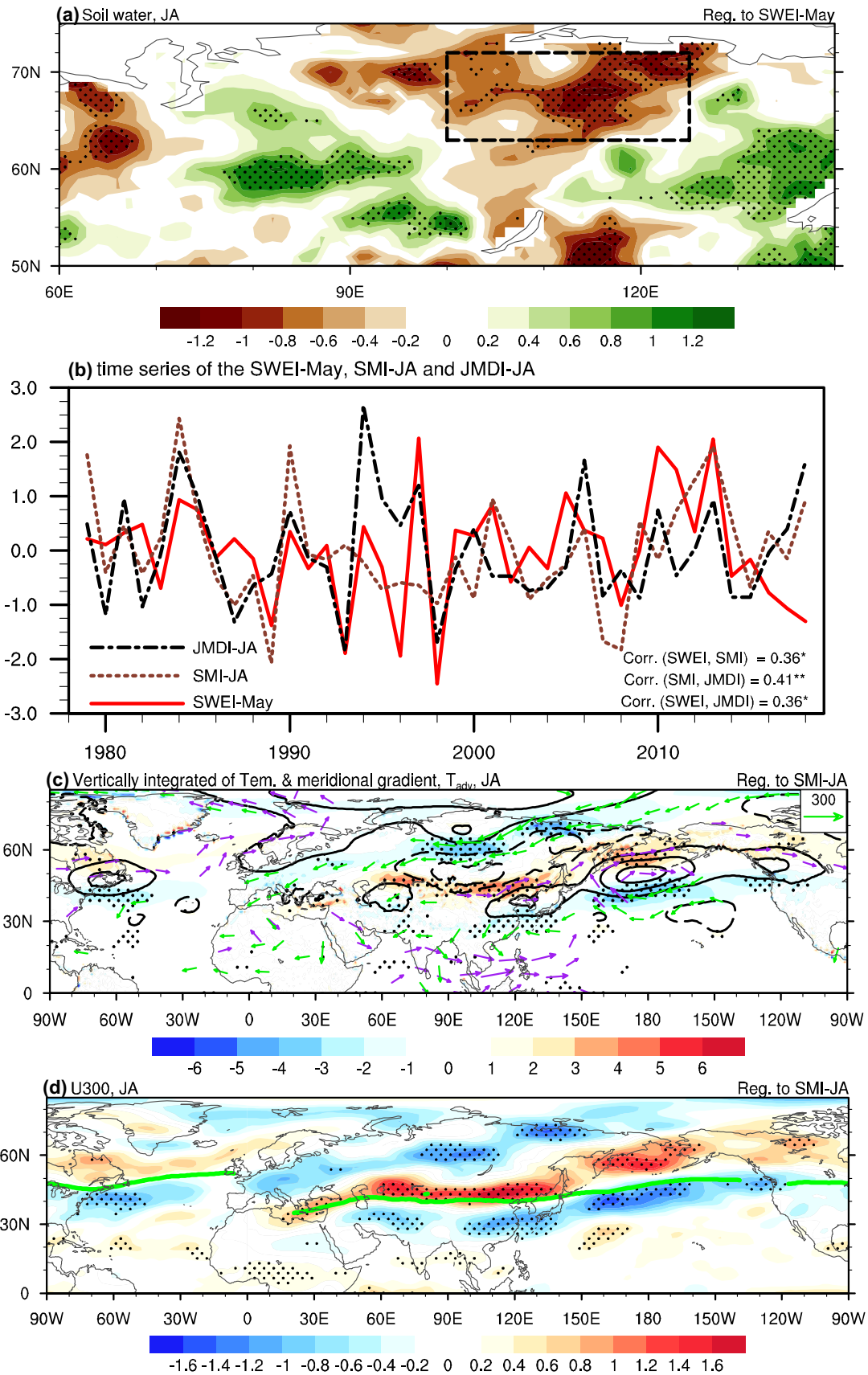
◀**Fig. 7 a** Regression of the top meter soil moisture anomalies (shading; 10^{-2} m^3 m^{-3}) in JA upon the SWEI in May during 1979–2018. **b** The time series of the SWEI in May (red solid line), the soil moisture index (SMI) in JA (coral dash line) and the JMDI in JA (black dash line). **c–d** Regressions of **c** temperature advection at 850 hPa (vectors; K m s^{-1}), vertically-integrated temperature (from 1000 to 200 hPa; contours; K) and its meridional gradient (shading; 10^{-2} K m^{-1}) anomalies in JA, and **d** zonal wind anomalies at 300 hPa (shading; m s^{-1}) in JA, upon the SMI in JA during 1979–2018. Contours in **c** are at $\pm 1, \pm 2, \pm 3, \pm 4 \times 10^4$ K. The purple (green) vectors in **c** delineate warm (cold) air advections, with only magnitude larger than 100 shown. Stippled values in **a**, **c**, **d** are significant at the 90% confidence level, based on the Student's t test

onto the SMI. When conditions of local drier soil prevail, the tropospheric temperature increases over the northern Siberia and East Asia-North Pacific sector and reduces over southern Siberia (Fig. 7c: contours). The anomalous temperature anomalies are associated with the cold and warm advections (Fig. 7c: vectors), which concur with the anticyclonic anomalies over northern Siberia through the positive feedback with the underlying drier soil (Fig. S6; Fischer et al. 2007). Consequently, negative temperature gradient anomalies are observed over 60° N and 30° N, in conjunction with positive anomalies over 45° N (Fig. 7c: shading). The zonal wind anomalies at 300 hPa regressed onto the SMI in Fig. 7d exhibits weakened westerly winds over 60° N and 30° N, and strengthened westerly winds over 45° N, which are consistent with the meridional temperature gradient anomalies. These upper-level zonal wind anomalies around the climatological Asian jet axis indicate a meridional (northward) displacement of the Asian jet (JMD; Lin and Lu 2005; Hong and Lu 2016). The JMD index (JMDI) is closely related to the SMI, and their correlation coefficient is 0.41 (above 99% confidence level, Fig. 7b).

Both the North Atlantic SSTAs and the Siberian soil moisture anomalies in JA are closely related to the SSC precipitation in JA. Based on the partial correlation coefficients, the relative contributions of the SST and the soil moisture to the SSC precipitation in JA are 5.8% and 16.8%, respectively. We thus define a Sea surface Temperature-soil Moisture index (STMI) in JA (Fig. 8a) better representing the combined effect of the North Atlantic SSTAs and the Siberian soil moisture. It is calculated based upon Corr. [SMI, SWEI] × SMI + Corr. [SSTI, SWEI] × SSTI, in which Corr. [SMI, SWEI] (Corr. [SSTI, SWEI]) means the correlation coefficient between SMI (SSTI) and SWEI. Figure 8b depicts the 200 hPa zonal and meridional wind anomalies regressed onto the STMI. In terms of the meridional wind, the wave train closely resembles the regression onto the SSTI (Fig. 6c), except over Eurasia where the SRP along the jet becomes much stronger and more significant. For the zonal wind (Fig. 8b: shading), it reproduces the northward JMD, consistent with the regression onto the SMI (Fig. 7d).

Therefore, the effects of the preceding SWE in May can be well represented by the STMI, which involves both the SRP and JMD, referred to as the upstream and downstream effects on SCC precipitation, respectively.

Figure 9 depicts the precipitation anomalies in JA regressed onto the PI, JMDI, SRPI and STMI. As expected, the JMDI-, SRPI- and STMI-regression patterns closely resemble that regressed onto the PI. All the three patterns display an apparently negative center of JA precipitation over SSC, although relatively weaker compared to the PI-related pattern. Furthermore, as shown in Fig. S7, the SRP is associated with the decreased water vapor primarily due to meridional wind anomalies. Meanwhile, the northward JMD regulates anomalous descending motion over SSC (also see Fig. 2). In addition, the regressions onto the SSTI and SMI similarly show a negative anomaly center over SCC, despite their weaker intensity (Fig. S8). It's notable that the precipitation anomalies over Inner Mongolia are also correlated with the Siberian SWE (Figs. 1b, 10e), which hasn't been discussed in this paper. Interestingly, the precipitation anomalies associated with the SSTI also show similar but weaker anomalies over Inner Mongolia (Figs. S8a and S8b). It suggests that the North Atlantic SSTAs may influence the precipitation anomalies over Inner Mongolia.

4 Conclusions and discussion

The previous studies have explored the relationship between Siberian SWE in Spring and the East Asian precipitation in summer (Wu et al. 2009; Zhang et al. 2017). However, in this study, we emphasize that the SST over the North Atlantic and the Siberian soil moisture have play important linking roles in the Siberian SWE–SCC precipitation connection. These physical processes can be described schematically as follows (also see Fig. S9):

- Corresponding to the below-normal Siberian SWE anomalies in May (Fig. 10a), over Siberia there is significant tropospheric warming from the surface into 400 hPa and largely positive 300 hPa geopotential height anomaly. It instigates the Rossby wave train originated over Siberia and propagating eastward across Pacific and toward the North Atlantic (Figs. 3, 4). The associated Atlantic jet weakens, following by a tripole pattern response of SSTAs over the North Atlantic (Fig. 5). It is noteworthy that, on the one hand, the May tripole pattern of SSTAs over the North Atlantic persists into JA to some extent (Fig. 10b), and on the other hand, the Siberian soil moisture in JA is drier-than-normal owing to less Siberian SWE in May–June (Fig. 10c).
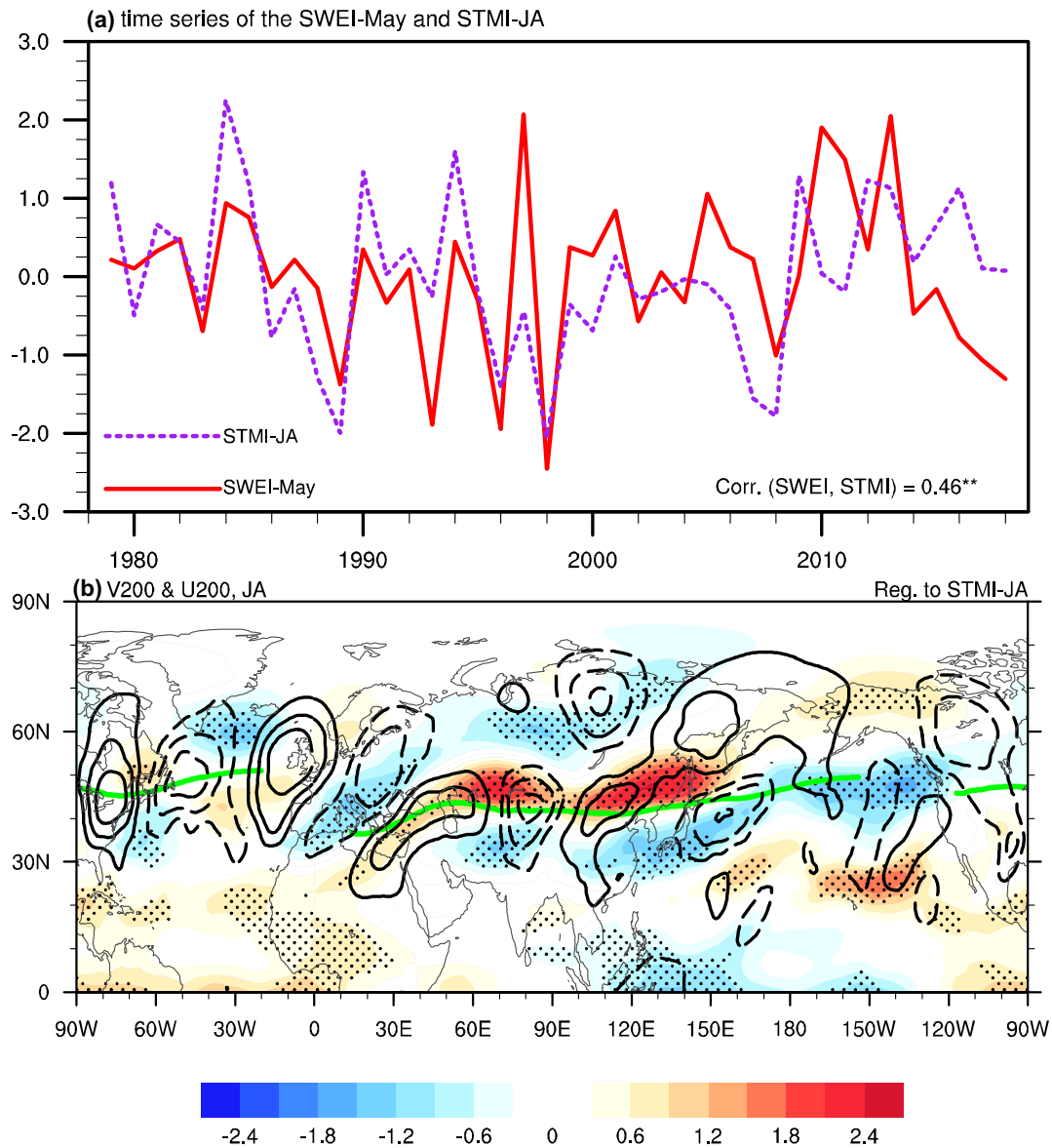
Fig. 8 a The time series of the SWEI in May (red solid line) and the sea surface temperature-soil moisture index (STMI) in JA (purple dash line). **b** Regressions of 200 hPa meridional wind (contours; m s^{-1}) and zonal wind (shading; m s^{-1}) anomalies in JA, upon the STMI in JA during 1979–2018. Contours in **b** are at ±0.4, ±0.8, ±1.2 m s^{-1}

- In JA, the SSTAs over the North Atlantic in turn may excite a Rossby wave train, referred as the SRP. It is characterized by the alternating northerly and southerly wind anomalies from the North Atlantic, along the southern slope of the Tibetan plateau and toward East Asia (Fig. 6). In addition, the drier Siberian soil concurs with an anomalous overlying anticyclone through the positive feedback (Fischer et al. 2007; Fig. S7). The associated cold air advection along the eastern and southern flanks of the anomalous anticyclone cools the tropospheric temperature over southern Siberia, which further favors the JMD by changing in the meridional temperature gradient (Fig. 7).

- The combination of the SRP and the JMD (i.e., the upstream and downstream effects, respectively; Figs. 8, 10d) contributes to less water vapor transport from the tropical ocean and anomalous descending motions
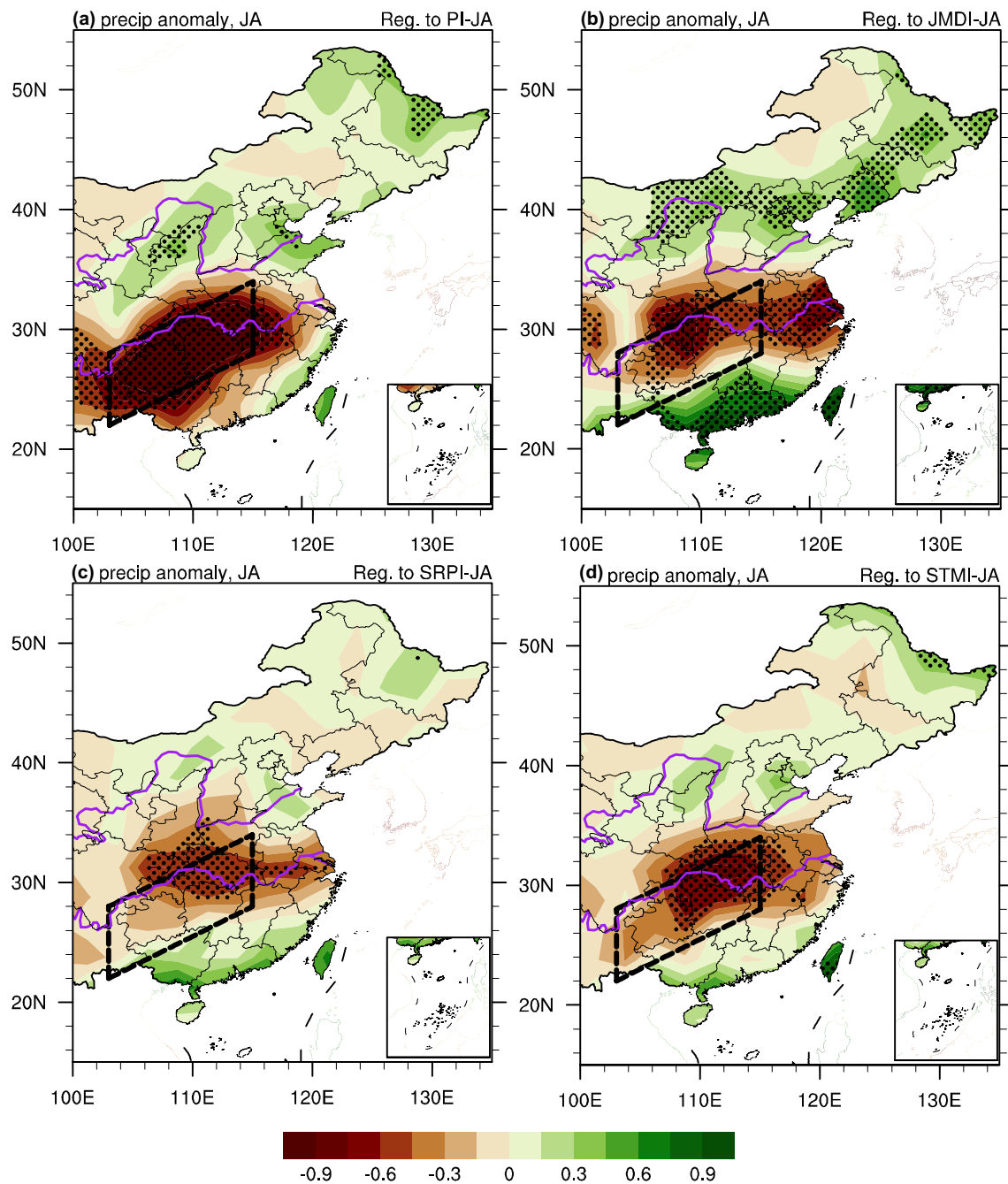
Fig. 9 Regression of JA precipitation anomalies (mm day^{-1}) in China east of 100° E upon **a** the PI in JA, **b** the JMDI in JA, **c** the SRPI in JA, and **d** the STMI in JA during 1979–2018. Stippled values are significant at the 90% confidence level, based on the Student's *t* test

around 25°–32° N, and hence the lack of precipitation in SCC (Figs. 2, 10e).

Fan et al. (2008) proposed a statistical model that can explain 64% of the interannual variability of the YRV summer precipitation, based on six predictors (Antarctic Oscillation, Ural circulation, East Asia circulation, meridional wind shear, South Pacific circulation, and low-level vorticity). The hybrid downscaling models, based on the simultaneous predictors from general circulation models (500 hPa geopotential height and 850 hPa specific humidity) and the preceding predictors from the reanalysis data (700 hPa geopotential height and sea level pressure), are also applied for the summer precipitation prediction over China (Liu and Fan
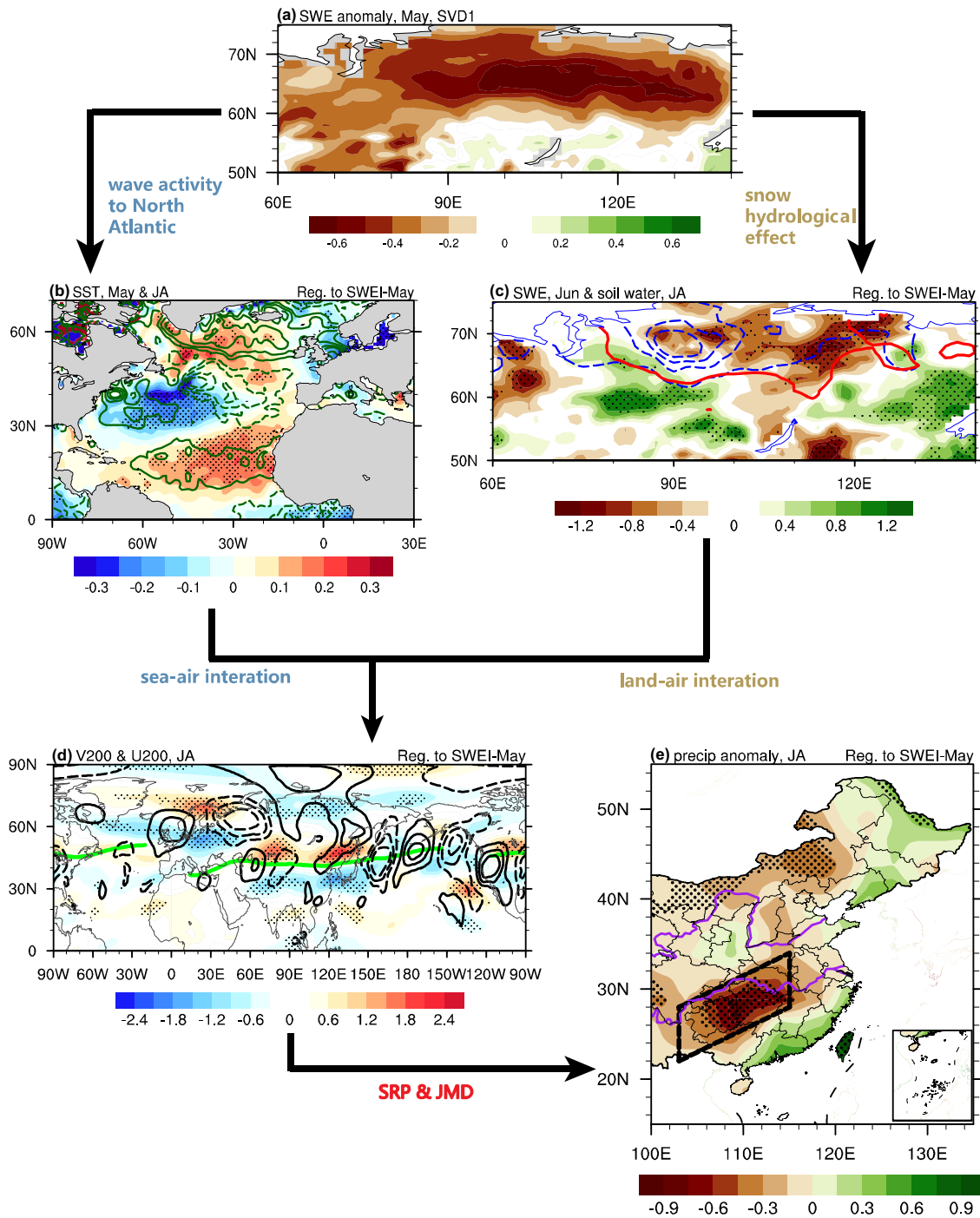
Fig. 10 Schematic diagram summarizing the dynamical linkage between the snow depth decrease over Siberia in May with the precipitation anomalies over SCC in JA. **a** Spatial distributions of SWE in May over Siberia of the leading SVD mode (as Fig. 1a); Regressions of **b** the SST anomalies in May (shading; K) and JA (contours; K); **c** the snow depth anomalies in June (contours; mm) and the top meter soil moisture anomalies in JA (shading; 10^{-2} m^3 m^{-3}); **d** the zonal wind anomalies (shading; m s^{-1}) and meridional wind anoma- lies (contours; m s^{-1}) at 200 hPa in JA; and **e** JA precipitation anoma- lies (shading; mm day^{-1}) in China east of 100° E, upon the SWEI in May during 1979–2018. Contours in **b** are at ± 0.05, ± 0.1, ± 0.15, ± 0.2 °C, in (**c**) are at -32, -22, -12, -2 mm and in **d** are at ± 0.4, ± 0.8, ± 1.2 m s^{-1}. The thick red line in **c** denotes the 90% confidence level of the SWE anomalies in June. Stippled values are significant at the 90% confidence level, based on the Student's t test

[2014](). However, these prediction models did not consider the effects of the preceding Siberian snowpack. Our study indicates that the May Siberian snow is closely related to the summer precipitation over SCC, and explains 23% of the total variance. Considering May SWE as a potential predictor can help improving the summer SCC precipitation predictability.

References

Balsamo G et al (2015) ERA-interim/land: a global land surface reanalysis data set. Hydrol Earth Syst Sci 19:389–407

Bamzai A, Marx L (2000) COLA AGCM simulation of the effect of anomalous spring snow over Eurasia on the Indian summer monsoon. Q J R Meteorol Soc 126:2575–2584

Bamzai AS, Shukla J (1999) Relation between Eurasian snow cover, snow depth, and the Indian summer monsoon: an observational study. J Clim 12:3117–3132

Barnett TP, Dümenil L, Schlese U, Roeckner E, Latif M (1989) The effect of Eurasian snow cover on regional and global climate variations. J Atmos Sci 46:661–686

Chen G, Huang R (2012) Excitation mechanisms of the teleconnection patterns affecting the July precipitation in Northwest China. J Clim 25:7834–7851

Cohen J, Rind D (1991) The effect of snow cover on the climate. J Clim 4:689–706

Cohen J, Barlow M, Kushner PJ, Saito K (2007) Stratosphere–troposphere coupling and links with Eurasian land surface variability. J Clim 20:5335–5343

Dash S, Singh G, Shekhar M, Vernekar A (2005) Response of the Indian summer monsoon circulation and rainfall to seasonal snow depth anomaly over Eurasia. Clim Dyn 24:1–10

Dash S, Parth Sarthi P, Panda S (2006) A study on the effect of Eurasian snow on the summer monsoon circulation and rainfall using a spectral GCM. Int J Climatol J R Meteorol Soc 26:1017–1025

Dee DP et al (2011) The ERA-interim reanalysis: configuration and performance of the data assimilation system. Q J R Meteorol Soc 137:553–597

Dickson RR (1984) Eurasian snow cover versus Indian monsoon rainfall—an extension of the Hahn–Shukla results. J Clim Appl Meteorol 23:171–173

Duan H, Wang S, Feng J (2013) The national drought situation and its impacts and causes in the summer 2013. J Arid Meteorol 31:633–640

Fan K, Wang H, Choi Y (2008) A physically-based statistical forecast model for the middle-lower reaches of the Yangtze River Valley summer rainfall. Chin Sci Bull 53:602–609

Fasullo J (2004) A stratified diagnosis of the Indian monsoon—Eurasian snow cover relationship. J Clim 17:1110–1122

Fischer EM, Seneviratne SI, Vidale PL, Lüthi D, Schär C (2007) Soil moisture–atmosphere interactions during the 2003 European summer heat wave. J Clim 20:5081–5099

Fletcher CG, Hardiman SC, Kushner PJ, Cohen J (2009) The dynamical response to snow cover perturbations in a large ensemble of atmospheric GCM integrations. J Clim 22:1208–1222

Groisman PY, Karl TR, Knight RW (1994) Observed impact of snow cover on the heat balance and the rise of continental spring temperatures. Science 263:198–200

Gu W, Li C, Wang X, Zhou W, Li W (2009) Linkage between mei-yu precipitation and North Atlantic SST on the decadal timescale. Adv Atmos Sci 26:101–108

Hahn DG, Shukla J (1976) An apparent relationship between Eurasian snow cover and Indian monsoon rainfall. J Atmos Sci 33:2461–2462

Halder S, Dirmeyer PA (2017) Relation of Eurasian snow cover and Indian summer monsoon rainfall: importance of the delayed hydrological effect. J Clim 30:1273–1289

Henderson GR, Peings Y, Furtado JC, Kushner PJ (2018) Snow–atmosphere coupling in the Northern Hemisphere. Nat Clim Change 8:954–963

Hong X, Lu R (2016) The meridional displacement of the summer Asian Jet, Silk Road pattern, and tropical SST anomalies. J Clim 29:3753–3766

Huang R, Chen W, Yang B, Zhang R (2004) Recent advances in studies of the interaction between the East Asian winter and summer monsoons and ENSO cycle. Adv Atmos Sci 21:407–424

Lin Z, Lu R (2005) Interannual meridional displacement of the East Asian upper-tropospheric jet stream in summer. Adv Atmos Sci 22:199

Linderholm HW et al (2011) Interannual teleconnections between the summer North Atlantic Oscillation and the East Asian summer monsoon. J Geophys Res Atmos 116:D13107

Liu Y, Fan K (2014) An application of hybrid downscaling model to forecast summer precipitation at stations in China. Atmos Res 143:17–30

Lu R-Y, Oh J-H, Kim B-J (2002) A teleconnection pattern in upper-level meridional wind over the North African and Eurasian continent in summer. Tellus A Dyn Meteorol Oceanogr 54:44–55

Meng L, Long D, Quiring SM, Shen Y (2014) Statistical analysis of the relationship between spring soil moisture and summer precipitation in East China. Int J Climatol 34:1511–1523

Orsolini YJ, Zhang L, Peters DH, Fraedrich K, Zhu X, Schneidereit A, van den Hurk B (2015) Extreme precipitation events over north China in August 2010 and their link to eastward-propagating wave-trains across Eurasia: observations and monthly forecasting. Q J R Meteorol Soc 141:3097–3105

Rayner N et al (2003) Global analyses of sea surface temperature, sea ice, and night marine air temperature since the late nineteenth century. J Geophys Res 108:1063–1082

Robock A, Mu M, Vinnikov K, Robinson D (2003) Land surface conditions over Eurasia and Indian summer monsoon rainfall. J Geophys Res Atmos 108:4131

Rossby T (1996) The North Atlantic current and surrounding waters: at the crossroads. Rev Geophys 34:463–481

Sardeshmukh PD, Hoskins BJ (1988) The generation of global rotational flow by steady idealized tropical divergence. J Atmos Sci 45:1228–1251

Shen H, He S, Wang H (2019) Effect of summer Arctic sea ice on the reverse August precipitation anomaly in Eastern China between 1998 and 2016. J Clim 32:3389–3407

Sun B (2017) Seasonal evolution of the dominant modes of the Eurasian snowpack and atmospheric circulation from autumn to the subsequent spring and the associated surface heat budget. Atmos Ocean Sci Lett 10:191–197

Sung MK, Kwon WT, Baek HJ, Boo KO, Lim GH, Kug JS (2006) A possible impact of the North Atlantic Oscillation on the east Asian summer monsoon precipitation. Geophys Res Lett 33:L21713

Takala M et al (2011) Estimating northern hemisphere snow water equivalent for climate research through assimilation of space-borne radiometer data and ground-based measurements. Remote Sens Environ 115:3517–3529

Takaya K, Nakamura H (2001) A formulation of a phase-independent wave-activity flux for stationary and migratory quasigeostrophic eddies on a zonally varying basic flow. J Atmos Sci 58:608–627

Tian B, Fan K (2012) Relationship between the late spring NAO and summer extreme precipitation frequency in the middle and lower reaches of the Yangtze River. Atmos Ocean Sci Lett 5:455–460

Walsh JE, Jasperson WH, Ross B (1985) Influences of snow cover and soil moisture on monthly air temperature. Mon Weather Rev 113:756–768

Wang H (2002) The instability of the East Asian summer monsoon–ENSO relations. Adv Atmos Sci 19:1–11

Wang B, Wu R, Fu X (2000) Pacific–East Asian teleconnection: how does ENSO affect East Asian climate? J Clim 13:1517–1536

Wang B, Liu J, Yang J, Zhou T, Wu Z (2009) Distinct principal modes of early and late summer rainfall anomalies in East Asia. J Clim 22:3864–3875

Wegmann M, Orsolini Y, Dutra E, Bulygina O, Sterin A, Brönnimann S (2017) Eurasian snow depth in long-term climate reanalyses. The Cryosphere 11:923–935

Wu B, Yang K, Zhang R (2009) Eurasian snow cover variability and its association with summer rainfall in China. Adv Atmos Sci 26:31–44

Xie P, Arkin PA (1997) Global precipitation: a 17-year monthly analysis based on gauge observations, satellite estimates, and numerical model outputs. Bull Am Meteorol Soc 78:2539–2558

Xie S-P, Hu K, Hafner J, Tokinaga H, Du Y, Huang G, Sampe T (2009) Indian ocean capacitor effect on Indo–Western Pacific climate during the summer following El Niño. J Clim 22:730–747

Xu L, Dirmeyer P (2011) Snow-atmosphere coupling strength in a global atmospheric model. Geophys Res Lett. https://doi.org/10.1029/2011GL048049

Xu L, Dirmeyer P (2013) Snow–atmosphere coupling strength. Part II: albedo effect versus hydrological effect. J Hydrometeorol 14:404–418

Xu B, Chen H, Sun S, Gao C (2018) Large discrepancy between measured and remotely sensed snow water equivalent in the northern Europe and western Siberia during boreal winter. Theor Appl Climatol 137:133–140

Yang J, Liu Q, Xie SP, Liu Z, Wu L (2007) Impact of the Indian Ocean SST basin mode on the Asian summer monsoon. Geophys Res Lett 34:L02708

Yasunari T, Kitoh A, Tokioka T (1991) Local and remote responses to excessive snow mass over Eurasia appearing in the northern spring and summer climate. J Meteorol Soc Jpn Ser II 69:473–487

Yim S-Y, Jhun J-G, Lu R, Wang B (2010) Two distinct patterns of spring Eurasian snow cover anomaly and their impacts on the East Asian summer monsoon. J Geophys Res 115:D22113

Zhang R, Zuo Z (2011) Impact of spring soil moisture on surface energy balance and summer monsoon circulation over East Asia and precipitation in East China. J Clim 24:3309–3322

Zhang YL, Li BY, Zheng D (2002) A discussion on the boundary and area of the Tibetan Plateau in China (Chinese). Geogr Res 21:1–8

Zhang R, Zhang R, Zuo Z (2017) Impact of Eurasian spring snow decrement on East Asian summer precipitation. J Clim 30:3421–3437

Zuo Z, Yang S, Zhang R, Xiao D, Guo D, Ma L (2015) Response of summer rainfall over China to spring snow anomalies over Siberia in the NCEP CFSv2 reforecast. Q J R Meteorol Soc 141:939–944